From design to characterization of zirconium nitride/silicon nitride nanocomposites

Mirna Chaker Bechelany, Vanessa Proust, Abhijeet Lale, Maxime Balestrat, Arnaud Brioude, Christel Gervais, Rafael Kenji Nishihora, Samuel Bernard

To cite this version:

Mirna Chaker Bechelany, Vanessa Proust, Abhijeet Lale, Maxime Balestrat, Arnaud Brioude, et al.. From design to characterization of zirconium nitride/silicon nitride nanocomposites. Journal of the European Ceramic Society, 2022, 42 (5), pp.2135-2145. 10.1016/j.jeurceramsoc.2022.01.007 . hal-03660916

HAL Id: hal-03660916
https://cnrs.hal.science/hal-03660916v1

Submitted on 6 May 2022

From design to characterization of zirconium nitride/silicon nitride nanocomposites

Mirna Chaker Bechelany [a], Vanessa Proust [b], Abhijeet Lale [b], Maxime Balestrat [c], Arnaud Brioude [a], Christel Gervais [d], Rafael Kenji Nishihora [c,*], Samuel Bernard [c,*]

[a] Univ Lyon, Université Claude Bernard Lyon 1, CNRS, Laboratoire des Multimatériaux et Interfaces, F-69622, Villeurbanne, France
[b] IEM (Institut Europeen des Membranes), UMR 5635 (CNRS-ENSCM-UM), Universite Montpellier, Place E. Bataillon, F-34095, Montpellier, France
[c] University of Limoges, CNRS, IRCER, UMR 7315, F-87000, Limoges, France
[d] Sorbonne Université, CNRS, Collège de France, Laboratoire Chimie de la Matière Condensée de Paris, 4 Place de Jussieu, 75005, Paris, France

ARTICLE INFO

Keywords:
Nanocomposites
Polymer-derived ceramics
Si_3N_4
ZrN
Optical properties

ABSTRACT

ZrN/Si_3N_4 nanocomposites have been prepared by chemically crosslinking two polysilazanes with a zirconium-based compound and subsequent heat-treatment at temperatures ranging from 1000 to 1600 °C. The polymer synthesis has been systematically investigated using FT-IR, solid-state NMR, and elemental analyses. Then, the pyrolysis under ammonia at 1000 °C trigering the thermo-chemical polymer-to-ceramic conversion was examined, leading to X-ray amorphous ceramics with yields governed by the chemistry of the neat polysilazane. Investigations of the structural evolution of the single-phase amorphous ceramic network above 1000 °C by X-ray diffraction and Raman spectroscopy pointed out that the ZrN phase already segregated at 1400 °C and formed highly crystalline ZrN/Si_3N_4 nanocomposites at 1600 °C. HRTEM investigations validated the unique nanostructural feature of the nanocomposites made of ZrN nanocrystals distributed in α- and β-Si_3N_4 phases. Our preliminary investigations of the optical properties showed that these structural changes allowed tuning the optical properties of ZrN/Si_3N_4 nanocomposites.

1. Introduction

Materials discovery plays a key role in the innovation cycle of energy conversion, transmission and storage technologies [1]. Among the different types of materials with high potential in energy-related fields, advanced ceramics - inorganic and non-metallic solids that represent an “advancement” over traditional ceramics (*e.g.*, porcelain) - exhibit unique and/or superior functional attributes that can be “precisely specified” by careful synthesis, processing and quality control. Because of the attention to microstructural design and the large possibilities of element combination which are known to enhance performance and to generate new physical phenomena, ceramics prepared at nanoscale, *i.e.*, nanoceramics [2], represent high value-added products that recently demonstrated attractivities in the energy fields [3–9]. Such nanoceramics can represent also a nanoscaled component of composite materials to form nanocomposites with completely novel property combinations, owing to the synergetic effects between the different components.

The synthesis of nanosized ceramics is quite challenging, particularly, *via* traditional powder route. In this regard, the PDC (Polymer-Derived Ceramics) route provides a flexible way to tailor the chemical composition of these ceramics at the molecular level. Several Si_3N_4-based nanocomposites have successfully been synthesized lately, covering a wide range of important applications. For instance, SiC/Si_3N_4 nanocomposite consists of a promising material for many engineering applications, such as turbine engines, high-performance cutting tools, and wear-resistant parts owing to their excellent mechanical properties and high oxidation and corrosion tolerance [10,11]. Another impactful research area is catalysis [12], which includes Transition Metal (TM) or TM Nitrides (TMN)/Si_3N_4 such as Co/Si_3N_4 [13], TiN/Si_3N_4 [14,15] and VN/Si_3N_4 [16] compounds. In particular, TiN/Si_3N_4 nanocomposites [15] demonstrated strong synergy between the nanoscaled TiN, the Si_3N_4 matrix and the Pt nanoparticles, which were homogeneously deposited onto the nanocomposite support in a second synthesis step. This resulted in excellent catalytic performances for dehydrogenation of sodium borohydride in water.

ZrN catalysts have been recently reported to outperform platinum (Pt) in alkaline conditions for oxygen reduction reactions (ORR) [17].

---

* Corresponding authors.
E-mail addresses: rafael.nishihora@hotmail.com (R.K. Nishihora), Samuel.bernard@unilim.fr (S. Bernard).

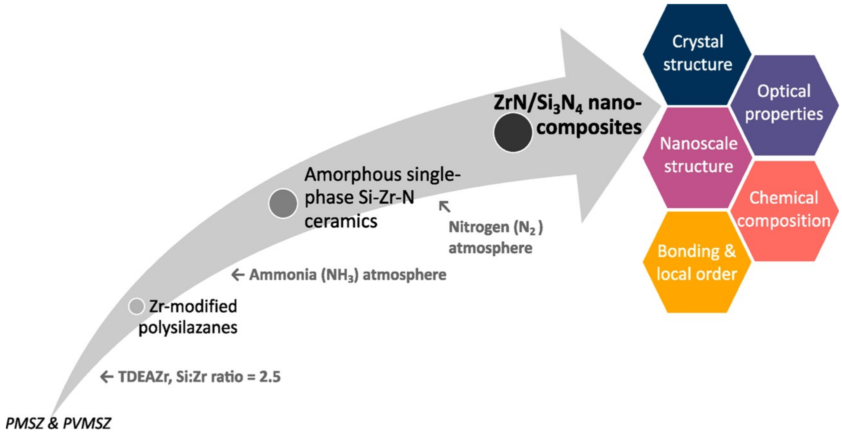

Fig. 1. Schematic diagram of the general process of designing ZrN/Si_3N_4 nanocomposites from Zr-modified polysilazanes and provided chemical, structural and optical fingerprints.

However, the synthesis of nanoscaled ZrN is highly challenging. In our process, the fact that nanoscaled ZrN is embedded in a covalently-bonded Si_3N_4 matrix – the latter acting as a support - will prevent pronounced coarsening and the damage of the dispersed nanoscaled ZrN, thus providing materials with high and constant performance even when exposed to high temperatures and/or harsh environmental conditions. Furthermore, based on our recent study, the TMN (TM Ṯi, Zr, Hf) nanophase can be accessible [15], as required for catalysis applications. Aside from their catalytic potential, TMN display unique optical properties and electronic structure intended – for instance - towards long-lasting, bio- and CMOS-compatible plasmonic and metasurface applications as well as an emerging class of nanophotonic materials [18]. For instance, ZrN and ZrN/SiO_xN_y have previously been shown to be effective plasmonic materials in the visible range, providing a low-cost alternative to gold and silver as well as wider application in harsh environments [19,20]. Thus, ZrN-based nanocomposites could offer strong interest for energy technologies through the exploitation of their optical, catalytic and electronic properties.

In this work, we have exploited the advantage of producing TMN/Si_3N_4 compounds [14,15,21–23] by the PDC route [24–37] to design ZrN/Si_3N_4 nanocomposites where their structure can be well controlled from the precursor level. Our approach involves first the synthesis of zirconium (Zr)-modified polysilazanes from liquid polysilazanes as Si_3N_4 precursors, *i.e.*, polymethylsilazane (PMSZ) and poly(vinyl- methyl-*co*-methyl)silazane (PVMSZ), which are known to deliver Si-C-N ceramics [22,38,39]. Then, we played with the reactivity of the central Si and Zr cations distributed in the polysilazane network with ammonia (used as atmosphere to form nitrides), resulting in an amorphous single-phase Si-Zr-N network at 1000 °C. The latter underwent subsequent phase separation and crystallization processes to deliver nanoscaled zirconium nitride (ZrN) clusters distributed in a Si_3N_4 matrix. At each stage of their synthesis, the materials have been systematically characterized. In addition, we provided preliminary optical property results of the nanocomposites. The present study demonstrates that the functional properties of the nanocomposites can be finely tuned by the unique chemistry of the nanocomposite precursors. The schematic representation of our approach is described in Fig. 1.

2. Experimental procedure

2.1. Materials

The synthesis of the precursor is carried out in a purified argon atmosphere passing through a column of phosphorus pentoxide and then a vacuum/argon line by means of standard Schlenk techniques. The cleaned glassware is stored in an oven at 90 °C overnight, before being connected to the vacuum/argon line, assembled and pumped under vacuum for 30 min, and then filled with argon. All chemical products are handled in an argon-filled glove box (MBraun MB200B for PMSZ; O_2 and H_2O concentrations kept at <0.1 ppm and Jacomex for PVMSZ, Campus-type; O_2 and H_2O concentrations kept at <0.1 ppm and 0.8 ppm, respectively). Toluene (99.85 %, Extra Dry over Molecular Sieve, AcroSeal(R)) was purchased from Acros Organics™. The poly(vinyl-methyl-*co*-methyl)silazane labelled PVMSZ (commercial name: Durazane® 1800) was provided by Merck company, Germany, stored in a fridge and used as-received. FTIR (ATR/cm^{-1}): ν (N–H) = 3388 (m), ν (C–H) = 3046 (w), 3010 (vs), 2954 (s), 2895 (s), 2852 (m), ν (Si-H) = 2121 (s), δ (vinyl) = 1591 (m) + 1405 (m), δ (Si-CH_3) = 1251 (s), δ (N-H): 1166 (m), δ (C=C + N–Si-N + C-H + Si-C) = 1005-630 (vs); ^1H NMR (300 MHz, $CDCl_3$, δ/ppm): 0.4–0.1 (br, $SiCH_3$), 1.1–0.5 (br, NH), 4.9–4.4 (br, SiH), 6.3–5.7 (br, vinyl). Polymethysilazane (PMSZ) was synthesized by ammonolysis of dichloromethylsilane (DCMS, $HSiCH_3Cl_2$) in accordance to procedures described in the literature.10,14 DCMS was obtained from Sigma-Aldrich and freshly distilled from magnesium at P_{atm} before use. FTIR (ATR/cm^{-1}): ν (N–H) = 3377 (m), ν (C–H) = 2960 (s), 2860 (m), ν (Si-H) = 2105 (s), δ (CH_x) = 1464 (m) + 1377 (m), δ (Si-CH_3) = 1251 (s), δ (N-H): 1174 (m), δ (N–Si-N + C-H + Si-C) = 1005-630 (vs). Tetrakis(diethylamino)zirconium ($Zr[N(CH_2CH_3)_2]_4$ (99 %) (labelled as TDEAZr) was obtained from ABCR GmbH, stored in a fridge and used without further purification.

2.2. Synthesis of zirconium-modified polysilazanes

The reaction between PMSZ/PVMSZ and TDEAZr is performed in toluene at temperature of reflux (115 °C) in a three-neck round-bottom flask. In a typical experiment using PVMSZ (which can be identically applied to the polymer synthesized from PMSZ), 3.0 g of TDEAZr (7.9 mmol) is added with a syringe under argon atmosphere to a solution of 1.30 g of PVMSZ (20.20 mmol referred to the monomeric unit of PVMSZ) in 150 mL of toluene at RT under vigorous stirring. When addition has ended, the temperature is increased up to 115 °C and kept at this temperature under vigorous stirring three days. After cooling down, the solvent is extracted *via* an ether bridge (100 °C/$1.5\cdot10^{-1}$ mbar) to release air- and moisture-sensitive from the zirconium-modified PVMSZ, which results in a yellow colored powder that is labelled as PVMZrSZ*2.5* (*2.5* being the Si:Zr ratio). Anal. Found (wt%): Si 19.6, Zr 19.3, C 31.2, N 16.3, H 7.2, O 6.4. $[Si_{1.0}Zr_{0.31}C_{3.7}N_{1.7}H_{10.3}O_{0.6}]_n$ (*Referenced to* $Si_{1.0}$ *in the empirical formulae*). FTIR (ATR/ cm^{-1}): ν(N–H) = 3388 (w), ν (C–H) = 3045 (w) + 2968 (vs) + 2925 (s), 2871 (s) + 2830 (m) + 2701 (w) + 2674 (w), ν(Si-H) = 2126 (s), δ (vinyl) = 1590 (m) + 1405 (m), δ(CH_x) = 1455 (m) + 1369 (m), ν(C-N) = 1290 (w), δ(Si-CH_3) = 1256 (s), δ (N-H, N–Si-N + C-H + Si-C) = 1184-

590 (vs). Based on the same synthesis procedure, the PMZrSZ2.5 is obtained as a brown powder. Anal. Found (wt %): Si 23.4, Zr 29.7, C 30.3, N 8.7, H 7.9, O 0.0. $[Si_{1.0}Zr_{0.37}C_{3.1}N_{0.8}H_{9.7}]_n$ (*Referenced to* $Si_{1.0}$ and *oxygen content was omitted in the empirical formulae*). FTIR (ATR/cm^{-1}): ν(N–H) = 3382 (m), ν (C–H) = 2960 (vs) + 2923 (s) + 2868 (s) + 2831 (m) + 2699 (w) + 2681 (w), ν(Si-H) = 2112 (s), δ(CH_x) = 1460 (m) + 1370 (m), ν(C-N) = 1290 (m), δ(Si-CH_3) = 1256 (s), δ (N-H, N–Si-N + C- H + Si-C) = 1182-590 (vs).

2.3. Preparation of the ceramic nanocomposites

Polymeric powders are placed in alumina boats in the glove-box, then introduced in a sealed tube under argon atmosphere to prevent any oxygen contamination of the samples during the transfer to the furnace. Powders are then introduced under argon flow into a silica tube from a horizontal furnace (Carbolite BGHA12/450B). The tube is evacuated (0.1 mbar) and refilled with anhydrous ammonia (99.99%) to atmospheric pressure. Subsequently, the samples are subjected to a cycle of ramping of 5 °C min^{-1} up to 1000 °C in flowing ammonia (dwelling time of 2 h at 1000 °C). A constant gas flow (120 mL min^{-1}) is passed through the tube during the pyrolysis cycle. After cooling under argon atmosphere, ammonia-pyrolyzed samples are stored in the glove-box for characterization. Samples are labeled PVMZrSZ*2.5*_10 or PMZrSZ*2.5*_10 (according to the nature of the polymer) with 10 being the two first digits of the temperature (1000 °C) at which the polymer has been exposed. For the high temperature (T > 1000 °C) investigation, samples pyrolyzed at 1000 °C are subsequently introduced in a graphite furnace (Gero Model HTK 8 for samples derived from PMSZ and VHT-GR from Nabertherm for samples derived from PVMSZ) for annealing treatments. The furnaces are pumped under vacuum (0.1 mbar), refilled with nitrogen and maintained under a constant flow of gas (200 mL min^{-1}) during the whole heat treatment. The program consists of a 5 °C min^{-1} heating ramp up to the maximum temperature fixed in the range 1400–1600 °C, dwelling at the selected temperature for 2 h and cooling down to RT at 5 °C min^{-1}. Samples are labelled PVMZrSZ*2.5*_T or PMZrSZ*2.5*_T with T the two first digits of temperature at which the material has been exposed (1400, 1500 and 1600 °C).

2.4. Material characterization

As the polymers are reactive towards moisture and oxygen, the following sample preparations were performed within a glove box. The chemical structure of the polymers was determined by transmission FTIR spectroscopy using a Nicolet Magna 550 Fourier transform-infrared spectrometer. ^{1}H NMR data of PMVSZ solutions in $CDCl_3$ were obtained using a Bruker AM 300 spectrometer operating at 300 MHz. Tetramethylsilane (TMS) was used as a reference for the NMR data. Solid-state ^{13}C CP MAS, ^{15}N CP MAS and ^{29}Si MAS NMR spectra were recorded on a Bruker AVANCE 300 spectrometer (7.0 T, $\nu_0(^{1}H)$ = 300.29 MHz, $\nu_0(^{13}C)$ = 75.51 MHz, $\nu_0(^{15}N)$ = 30.44 MHz, $\nu_0(^{29}Si)$ = 59.66 MHz) using a 7 mm Bruker probe spinning at 5 kHz. ^{13}C and ^{15}N CP MAS experiments were recorded with ramped-amplitude cross-polarization in the ^{1}H channel to transfer magnetization from ^{1}H to ^{13}C and ^{15}N. (Recycle delay = 3 s, CP contact time = 1 ms, optimized ^{1}H spinal- 64 decoupling). Single pulse ^{29}Si MAS NMR spectra were recorded with a recycle delay of 60 s. Chemical shift values were referenced to tetramethylsilane for ^{13}C and ^{29}Si and CH_3NO_2 for ^{15}N. Spectra were fitted with the DMFit program [40]. Chemical analyses of the polymers were performed using a combination of several methods at Mikroanalytisches Labor Pascher (Remagen, Germany). Thermogravimetric analyses (TGA) of samples were performed in flowing ammonia (50 mL min^{-1}) at 5 °C min^{-1} to 1000 °C using silica crucibles (Setaram TGA 92 16.18, SETARAM Instrumentation (Caluire, France)). The phase composition of ceramic samples was determined by XRD analysis (Bruker AXS D8 Discover, Cu$K\alpha$ radiation, Billerica, Massachussets, USA). The scans were performed in the range of $2\theta \in \langle 20^\circ; 90^\circ \rangle$ with a step of 0.015 ° and an exposure time of 0.7 s. The diffractograms were analyzed using the Diffrac EVA software with the JCPDS-ICDD database. Crystallite sizes of ZrN crystals were calculated from the FWHM of the (111) diffraction lines using the Scherrer formula while their chemical composition was measured by considering the interlayer spacing d_{111}. Raman spectroscopy microanalysis was achieved between 100 and 1500 cm^{-1} (Raman LabRAM ARAMIS) using an excitation He/Ne laser wavelength of 633 nm. For Transmission electron Microscopy (TEM, TOPCON 002B working at 200 kV) study, as-prepared nanocomposite powders were crushed under n-butanol in an agate mortar and deposited the drops onto a holey carbon membrane supported by a copper grid. The Selected Area Electron diffraction (SAED) patterns and images were recorded, using a TECNAI 30G^{2} microscope working at 300 kV. Optical characterization was carried out by using a UV–vis diffuse reflectance spectrophotometer (Perkin-Elmer UV/Visible spectrophotometer (lambda 35)) by recording the diffuse reflectance spectra of the nanocomposites then converted to absorbance by the Kubelka-Munk function in the wavelength range of 200–1100 nm.

3. Results and discussion

3.1. Nanocomposite precursor design

As described in the experimental section, the synthesis of the nanocomposite precursors consists in performing the reaction between polysilazanes as Si_3N_4 precursors and a low molecular weight compound (tetrakis(diethylamino)zirconium, TDEAZr) acting both as a ZrN precursor and a crosslinker at reflux of toluene (staying then three days). Zr-modified polysilazanes called polyzirconosilazanes, are thus generated. To understand and control the chemistry behind the precursor synthesis, we have synthesized two representative polyzirconosilazanes labelled PMZrSZ*2.5* and PVMZrSZ*2.5* (*2.5* indicates the Si:Zr atomic ratio) from PMSZ and PVMSZ, respectively. Both propose a controlled Si:Zr molar ratio which is fixed at 2.5 according to the quantity of TDEAZr added to PMSZ and PMVSZ solutions at RT prior to thermolysis. The elemental analysis data of PMZrSZ*2.5* $[Si_{1.0}Zr_{0.37}C_{3.1}N_{0.8}H_{9.7}]_n$, and PVMZrSZ*2.5* $[Si_{1.0}Zr_{0.31}C_{3.7}N_{1.7}H_{10.3}O_{0.6}]_n$ samples prove that the precursor synthesis proceeded as planned; in particular for the PMZrSZ*2.5* sample: the Si: Zr ratio measured by elemental analysis (2.7) is close to the one fixed during the synthesis (2.5). The non-negligible deviation between the Si: Zr ratio measured (3.3) and the one fixed (2.5) for PVMZrSZ*2.5* indicates that the TDEAZr introduced during the polymer synthesis did not completely react with PVMSZ. Most probably, the steric hindrance imposed by vinyl groups in PVMSZ limits the reaction of the latter with TDEAZr in comparison to PMSZ, which does not exhibit organic groups with such a steric hindrance per monomeric units. This is confirmed by the use of perhydropolysilazane (PHPS, $[SiH_2NH]_n$) as a Si_3N_4 precursor: a Si:Zr ratio of 2.5 has been measured (*results not published*). Beside this, carbon and hydrogen content significantly increased (more limited for the nitrogen content) in PMZrSZ*2.5* and PVMZrSZ*2.5* compared to neat polysilazanes ($[Si_{1.0}C_{1.5}N_{1.1}H_{5.5}]_n$ for PVMSZ (*Referenced to* $Si_{1.0}$ and *oxygen content – 0.4 wt% - was omitted in the empirical formulae*)) suggesting the presence of side groups such as $-[N(R)_2]_3$ (R = CH_2CH_3) units as in general shown with polysilazanes containing amino groups [39,41,42]. This could explain the extremely high sensitivity of these precursors to oxygen. In order to obtain a complete view of the precursor structure, the Zr-modified polysilazanes have been characterized by infrared and solid-state NMR spectroscopies.

The FTIR spectra of PMZrSZ*2.5* and PVMZrSZ*2.5* (See Fig. 1SI in ESI) display the characteristic absorption bands of neat PMSZ and PVMSZ, which share many features in common given their similar chemical structure: the stretching of N–H bonds at 3382—3388 cm^{-1} coupled to NH deformations at 1182–1184 cm^{-1}, the stretching of CH— bonds in CH_x groups at 2960–2968 and 2850—2871 cm^{-1}. The bands at 2112—2126 cm^{-1} and at 1256 cm^{-1} are attributed to stretching of Si–H bonds and deformations of SiC—H_3 units, respectively. Below ~1000

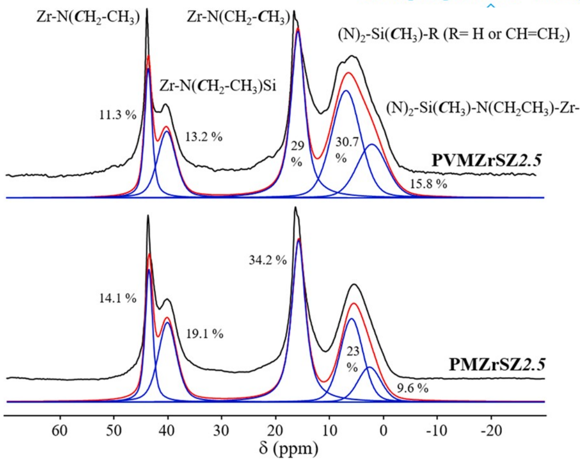

Fig. 3. Experimental and simulated ^{13}C CP MAS NMR spectra recorded for PMZrSZ*2.5* and PVMZrSZ*2.5*.

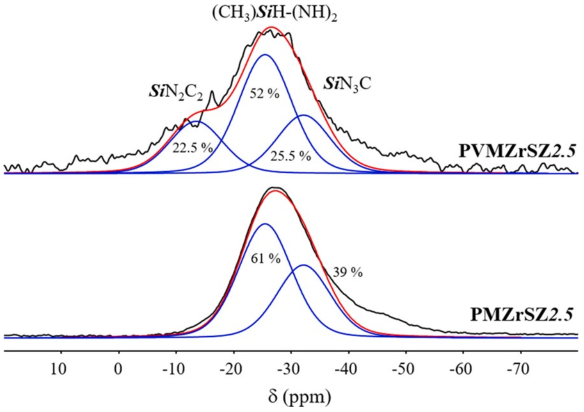

Fig. 4. (a) Experimental and simulated ^{29}Si MAS NMR spectra recorded for PMZrSZ*2.5* PVMZrSZ*2.5*.

cm^{-1}, absorption bands attributed to the stretching and deformation vibrations involving Si—C, Si-N, C-H, and ——C-C bonds, overlap and cannot be assigned unambiguously.

The main changes in both synthesized materials (PMZrSZ*2.5* and PVMZrSZ*2.5*) occur in the intensity of the main reaction sites as highlighted in Fig. 2. Hence, the bands assigned to N−H and SiH− bonds tend to shrink, with the band assigned to N−H bonds decreasing the most. Moreover, the bands assigned to the vibration of −C-H bond in the vinyl groups present only in PVMSZ decrease in intensity in the FTIR spectrum of PVMSZr*2.5*, suggesting that polymerization of the vinyl groups (reaction (3) in Fig. 2) and/or the hydrosilylation reaction

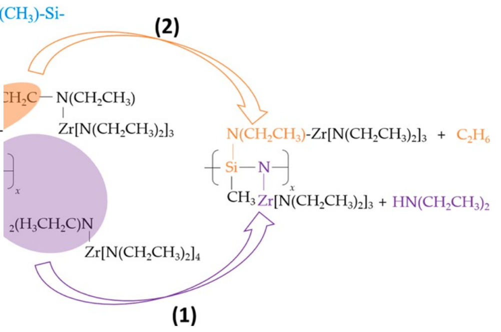

g the reaction between polysilazanes and TDEAZr.

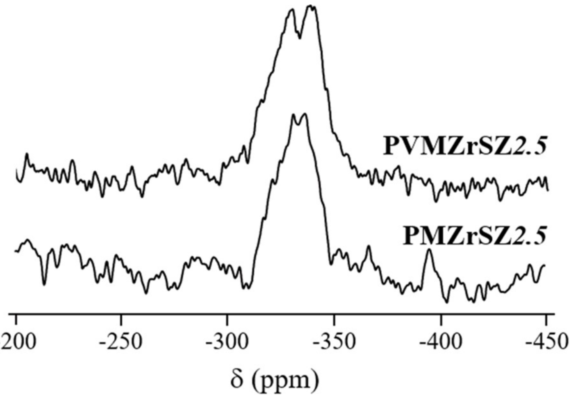

Fig. 5. Experimental ^{15}N CP MAS NMR spectra recorded for PMZrSZ*2.5* and PVMZrSZ*2.5*.

between —SiH and SiCHC———H$_2$ units, leading to the formation of carbosilane bonds (—SiCCSi;——— reaction (4) in Fig. 2) occur during the reaction. Parallel to the aforementioned events, a set of broad bands in the range of 2670–2860 cm^{-1} appears for both samples: they are attributed to the vibration of C—H bonds from TDEAZr's ethyl groups. The N—C bonds in NC—H$_2$CH$_3$ groups are responsible for the weakly intense band at 1290 cm^{-1}. At around 1370 cm^{-1}, another set of bands that can be ascribed to C—H band deformation appears.

As expected, FTIR spectroscopy tends to corroborate the involvement of NH and SiH groups in polysilazanes during the reaction of the latter with TDEAZr through the occurrence of the mechanism already identified during the reaction between PMSZ and tetrakis(dimethylamino) titanium (Ti[N(CH$_3$)$_2$]$_4$) labelled TDMATi [14,23]:

i) those involving -NH units in both polysilazanes and -N(CH$_2$CH$_3$)$_2$ groups in TDEAZr to form -N-Zr- bonds releasing ethylamine according to the reaction (1) in Fig. 2.
ii) those involving the silicon centers of polysilazanes and -N(CH$_2$CH$_3$)$_2$ groups in TDEAZr causing the consumption of Si-H groups while forming -Si-N(CH$_2$CH$_3$)-Zr- bridges in the obtained precursor and the concomitant evolution of ethane according to the reaction (2) in Fig. 2.

To achieve an in-depth understanding of the local carbon, nitrogen and silicon environments in the polymer, we investigated ^{13}C, ^{29}Si and ^{15}N *via* solid-state NMR spectroscopy of both polymers (Figs. 3–5). The cross-polarization (CP) technique has been used for ^{13}C and ^{15}N NMR experiments to obtain spectra with reasonable acquisition times and signal-to-noise ratios. Deconvolution of signals has been done for ^{13}C and ^{29}Si spectra of the PVMZrSZ*2.5* and PMZrSZ*2.5* samples, allowing reaching the site fraction of the different environments. Note that Table 1 summarizes the main findings regarding the chemical

Table 1
Summary of the NMR spectroscopy data of the PVMZrSZ*2.5* and PMZrSZ*2.5* samples.

Nucleus	Assignment	δ (ppm)	Deconvoluted fraction (%)	
			PVMZrSZ*2.5*	PMZrSZ*2.5*
^{13}C	(N)$_2$-Si(CH$_3$)-N(CH$_2$CH$_3$)-Zr-	2	15.8	9.6
	(N)$_2$-Si(CH$_3$)-R (R = H or CH = CH$_2$)	5	30.7	23.0
	Zr-N(CH$_2$-CH$_3$)	16	29.0	34.2
	Zr-N(CH$_2$-CH$_3$)Si	39	13.2	19.1
	Zr-N(CH$_2$-CH$_3$)	42	11.3	14.1
^{29}Si	SiN$_2$C$_2$	−13.5	22.5	———
	(CH$_3$)SiH-(NH)$_2$	−25.5	52.0	61.0
	SiN$_3$C	−32.5	25.5	39.0
^{15}N	HNSi$_2$	−335	*	*
	N-CH$_2$CH$_3$	−345	*	———

* Signal identified but not quantified.

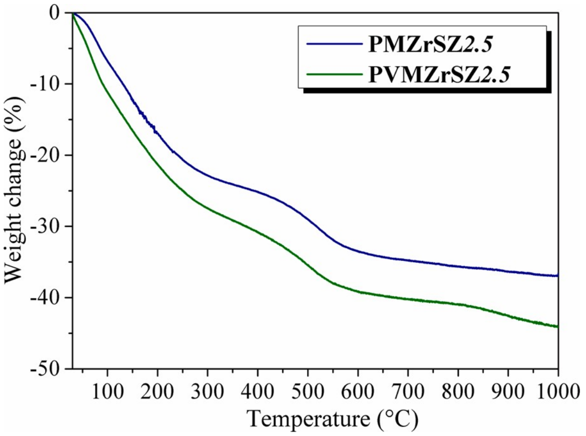

Fig. 6. TG curves recorded during decomposition of PMZrSZ*2.5* and PVMZrSZ*2.5* samples in flowing ammonia.

environments and the quantified deconvoluted signals (^{13}C and ^{29}Si) from the NMR analyzed samples.

The solid-state ^{13}C CP MAS NMR spectra (Fig. 3) exhibit four signals at around 5, 18, 39 and 42 ppm; the first one – very broad – being deconvoluted into two signals, one at 2 ppm and another one at 5 ppm.

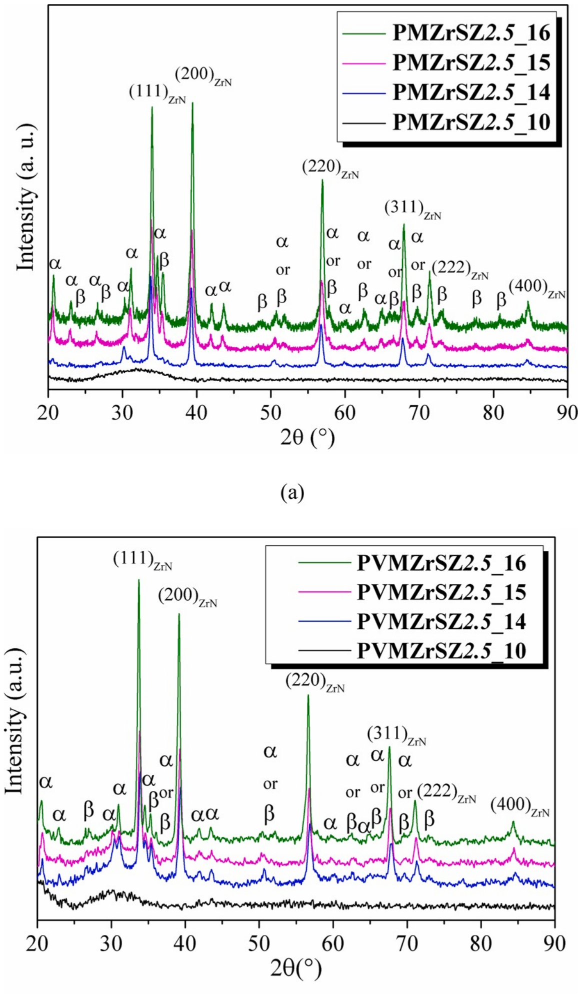

(a)

(b)

Fig. 7. XRD patterns of ceramics derived from PMZrSZ*2.5* (a) and PVMZrSZ*2.5* (b) samples prepared in flowing ammonia (up to 1000 °C) then in flowing nitrogen (1400-1600 °C).

Fig. 8. PMZrSZ*2.5*_14, PMZrSZ*2.5*_15, PMZrSZ*2.5*_16, and PMZrSZ*2.5*_17 samples from left to right.

^{13}C NMR signals around 0 ppm are generally assigned to carbon atoms of aliphatic groups bonded to a silicon atom, *i.e.* in this case Si*C*H$_3$ units as identified in PVMSZ (See Fig. 2SI in ESI) [38,39]. The presence of two signals can be due to the two types of SiCH$_3$ unit-containing environments shown in Fig. 2: SiCH$_3$ groups can be in SiCN$_3$ environments (*i.e.*, Si environment in the chain of the type $_2$(RN)-Si(CH$_3$)-N(CH$_2$CH$_3$)-Zr- because of the reaction of -SiH units with TDEAZr, reaction (2), Fig. 2) and in Si*C*RN$_2$ environment (with R = H (*i.e.*, Si environment in the monomeric unit of the type Si(CH$_3$)(H)(NH)$_2$ in PMSZ and PVMSZ) or R = C (*i.e.*, Si environment in the monomeric unit of the type Si(CH$_3$)(CH CH$_2$)(NH-)$_2$ of PVMSZ). Signals around 16 ppm can possibly be attributed to carbon atoms linked to another aliphatic carbon, in this case *C*H$_3$ environments of the N(CH$_2$CH$_3$)groups present in TDEAZr. The resonances at 39 and 42 ppm are assigned to carbon atoms linked to nitrogen; thereby N(*C*H$_2$CH$_3$)units in two types of environments [14,40]. Based on our previous report [23], resonances at 39 and 42 ppm are assigned to Zr-N(*C*H$_2$CH$_3$) units as side groups, *i.e.*, Si$_2$N-Zr-(N(*C*H$_2$CH$_3$)$_2$)$_n$ units (1 ≤ n ≤ 3) and as bridges, *i.e.*, $_2$(RN)-Si (CH$_3$)-N(CH$_2$CH$_3$)-Zr- units resulting from the reaction between SiH groups and TDEAZr, respectively. Consistently, the sum of both Zr-N*C*H$_2$- signals around 40 ppm is more or less equal to the Zr-N (CH$_2$*C*H$_3$) one around 16 ppm. At a given Si:Zr ratio (2.5), the relative proportion of the signal at 42 ppm compared to the one at 39 ppm is higher in PVMZrSZ*2.5* (0.856) in contrast to PMZrSZ*2.5* (0.738). This means that the reaction involving Si-H bonds is more efficient in the latter which is related to the fact that vinyl groups - imposing a certain steric hindrance in PVMSZ - are absent in the monomeric unit of PMSZ. Indeed, the ^{13}C signals at 124 and 138 ppm (See Fig. 3SI in ESI) in the PVMZrSZ*2.5* spectrum assigned to vinyl groups are already present in PVMSZ (See Fig. 3SI in ESI). Residual vinyl groups – which have been identified by FTIR in the sample - can provide a source of latent reactivity during the further thermo-chemical conversion of the PVMZrSZ*2.5* sample (*See later*). To complete our investigation, the experimental solid-state ^{29}Si MAS NMR spectra of PMZrSZ*2.5* and PVMZrSZ*2.5* have

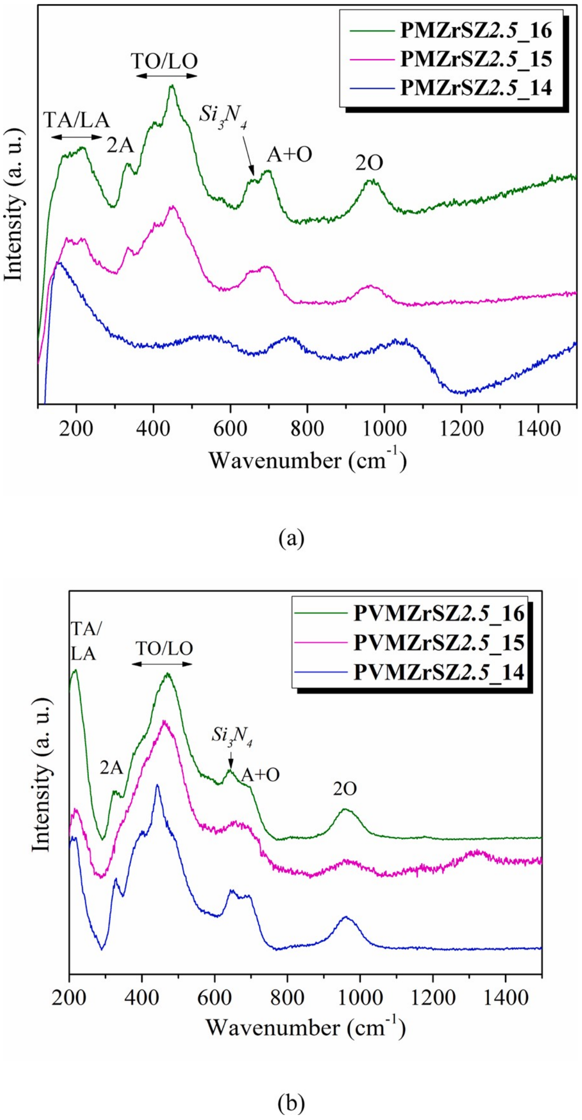

Fig. 9. Raman spectra of ceramics derived from PMZrSZ*2.5* (a) and PVMZrSZ*2.5* (b) samples prepared in flowing ammonia (up to 1000 °C) then in flowing nitrogen (1400–1600 °C).

been recorded at 7 T (Fig. 4).

In both samples, the ^{29}Si MAS spectra exhibit a main broad resonance centered at around −28 ppm that can be simulated with two or three components for PMZrSZ*2.5* and PVMZrSZ*2.5* respectively. The main signal at −25.5 ppm (is consistent with previously published results and attributed to silicon atoms in a *Si*HCN$_2$, *i.e.*, (CH$_3$)SiH-(NH)$_2$, environment [41–43]. The second signal at −32.5 ppm could correspond to *Si*N$_3$C, *i.e.*, $_2$(RN)-Si(CH$_3$)-N(CH$_2$CH$_3$)-Zr, environments highlighting reactions between Si-H units and N(CH$_2$CH$_3$)$_2$ groups (reaction (2), Fig. 2). For PVMZrSZ*2.5*, an additional signal is observed at −13.5 ppm, which can be assigned to *Si*N$_2$C$_2$ units. This chemical shift indicates that this sample is preferentially composed of six- and eight-membered Si-N rings [44]. The small signal present in both samples around −48 ppm can be attributed to *Si*N$_4$ groups [45], confirming the occurrence of a reaction between Si-H units and N(CH$_2$CH$_3$)$_2$ groups. The solid-state ^{15}N CP MAS NMR spectra (Fig. 5) of the same polymers display a very broad signal centered at −335 ppm, implying the presence of H*N*Si$_2$ environments in the silazane backbone in both samples [14,46]. Moreover, more resolution is observed in the PVMZrSZ*2.5* spectrum, indicating the presence of a second contribution around −345 ppm that would correspond to *N*(CH$_2$CH$_3$)environment.

The combination of multinuclear solid-state NMR data with the results derived from elemental analyses and FTIR allows for a comprehensive understanding of the chemistry behind the reaction between PMSZ/PVMSZ and TDEAZr. Two reactions depicted in Fig. 2 and involving TDEAZr occur during the synthesis of PMZrSZ*2.5* and PVMZrSZ*2.5*. Zr atoms are homogeneously distributed within the PMSZ/PVMSZ structures as bridges *i.e.* those involving -(Si-N)$_n$-Zr-units, which are built by the reaction between -N(CH$_2$CH$_3$)$_2$ from TDEAZr and -NH groups from PMSZ/PVMSZ; and those involving N$_2$Si (CH$_3$)-N(CH$_2$CH$_3$)-Zr- units, which arise due to the reaction between -SiH (from PMSZ/PVMSZ) and -N(CH$_2$CH$_3$)$_2$(from TDEAZr) moieties. The latter seems to be particularly active in the studied polymeric systems. As-formed units should allow building the polymer network of the samples and increase the degree of cross-linking of the polymeric backbone, which is a pre-requisite to limit the weight loss occurring during the further polymer-to-ceramic conversion. It should be pointed out that a third mechanism – involving TDEAZr not as a reagent but as a catalyst – occurred the hydrosilylation of vinyl groups of PVMSZ. Thus, once these precursors have been synthesized, the subsequent thermo-chemical conversion up to 1000 °C will occur in ammonia to deliver single-phase amorphous ceramics labelled as PMZrSZ*2.5*_10 and PVMZrSZ*2.5*_10 samples.

3.2. Ceramic conversion

The conversion of PMZrSZ*2.5* and PVMZrSZ2.5 into their single-phase amorphous ceramic derivatives (*i.e.*, PMZrSZ2.*5*_10 and PVMZrSZ*2.5*_10 samples) has been monitored by thermogravimetric analysis (TGA) as shown in Fig. 6.

The TG curves of the PMZrSZ*2.5* and PVMZrSZ*2.5* samples display a marked three-step weight loss in the temperature range 30–1000 °C. The first weight loss from 30 to 250 °C; a second one from 250 to 600 °C; and the third weight loss from 600 to 1000 °C. Whereas PMZrSZ*2.5* is decomposed with a weight loss much lower than that measured for PMSZ in the same conditions (85.25 % of weight loss at 1000 °C), the PVMSZZr*2.5* sample undergoes a weight loss measured at 1000 °C higher than that measured for PMVSZ (32.8 % of weight loss at 1000 °C) in flowing ammonia.

In both systems, the degree of crosslinking of the polymers after modification with Zr is higher than in neat polysilazanes according to the identified formation of bridged bonds such as direct bonds -N-Zr- (reaction (1) in Fig. 2) and -Si-N(CH$_3$)-Zr- (reaction (2) in Fig. 2). Such units are expected to reduce the segment mobility of PMSZ and PVMSZ hindering depolymerization reactions in the polysilazane network in the low temperature regime of the polymer-to-ceramic conversion; thereby, reducing the weight loss at low temperature. This clearly happens with PMZrSZ*2.5*. However, a high cross-linking is not the only prerequisite for a high yield polymer-to-ceramic conversion of preceramic polymer. Another important issue is a sufficient latent reactivity of the precursors, *i.e.*, the ability to undergo cross-linking reactions during the heat treatment. This is particularly the case when -Si-H, -N-H and vinyl groups are present in the polymer structure like in PVMSZ, which lead to dehydrocoupling and hydrosilylation reactions [47,48]. Because they reacted with TDEAZr during the polymer synthesis, the availability of such units is significantly reduced in the PVMZrSZ*2.5* sample compared to PVMSZ. Furthermore, the highest weight loss recorded for PVMZrSZ*2.5* is most probably a consequence of the presence of -N (CH$_2$CH$_3$)$_2$ as side groups in its structure. Such groups are unable to undergo cross-linking reactions and are decomposed during the polymer-to-ceramic conversion. Thus, PVMZrSZ*2.5* exhibits a more pronounced weight loss than PVMSZ because -N[(CH$_2$CH$_3$)$_x$]$_y$ units (x = 1 or 2 and y = 1→3) are highly reactive with ammonia to release amines as gaseous by-products *via* transamination reactions.

After the thermo-chemical conversion of the precursors at 1000 °C (dwelling time of 2 h) in flowing ammonia, the XRD patterns of the PMZrSZ*2.5*_10 and PVMZrSZ*2.5*_10 samples reveal that these 'SiZrN'

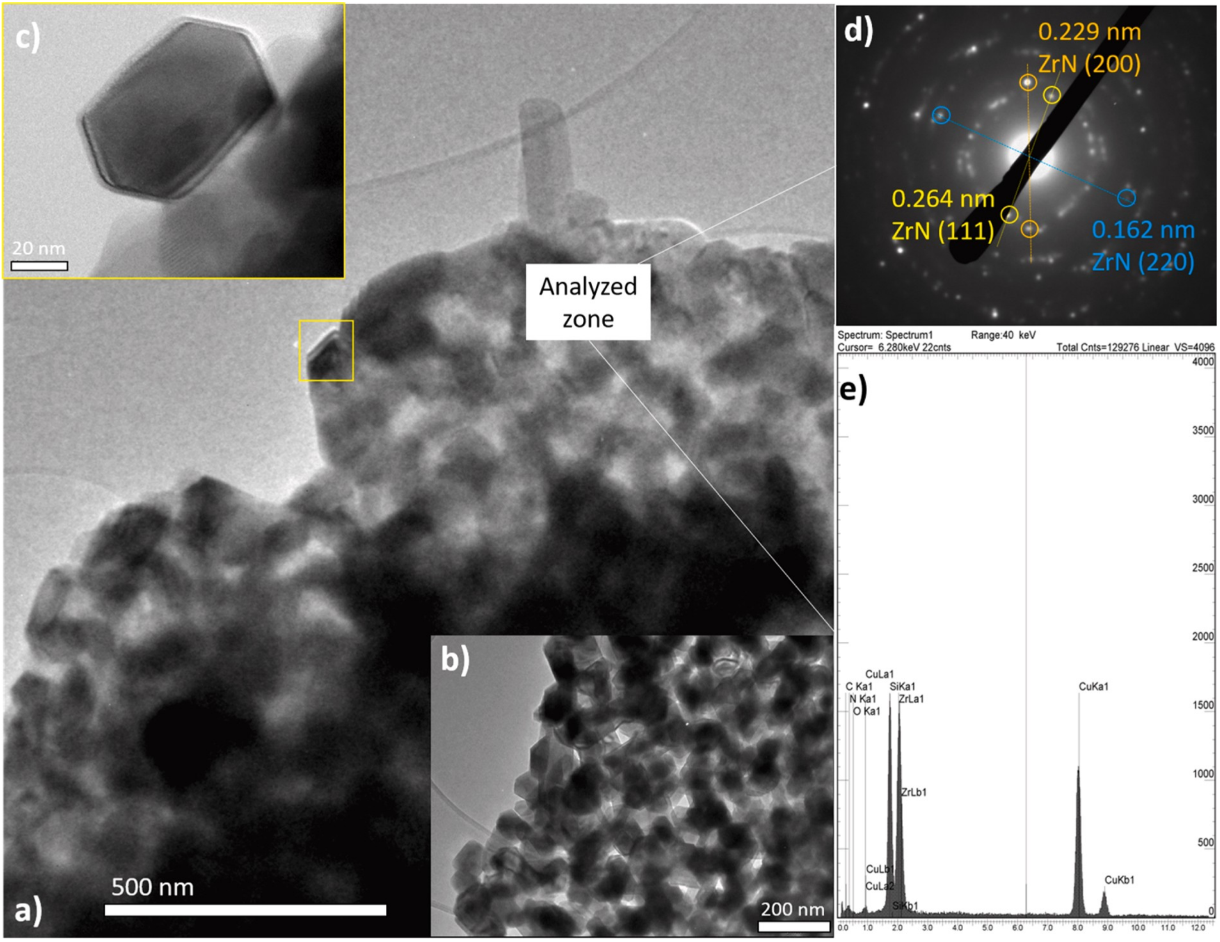

Fig. 10. (a,b) Low magnification TEM image of the surface of the PMZrSZ2.5_16 sample, c) TEM image of a ZrN nanocrystal, d) Selected area electron diffraction pattern and e) EDS map of the analyzed zone.

ceramics are amorphous as indicated by the diffuse XRD peaks composing the patterns (black lines in Fig. 7). Thus, higher temperatures have been applied to generate the title materials.

3.3. *High-Temperature phase and microstructure evolution*

The amorphous PMZrSZ2.5_10 and PVMZrSZ2.5_10 samples have been annealed at 1400 ˚C, 1500 ˚C, and 1600 ˚C for 2 h in nitrogen atmosphere in order to explore their high-temperature behaviour with respect to crystallization, phase separation and microstructure evolution.

Fig. 8 shows the changes in the colour of the samples produced from PMZrSZ2.5: PMZrSZ2.5_14, PMZrSZ2.5_15, PMZrSZ2.5_16. Note that the PMZrSZ2.5_17 sample is also presented although not being investigated in the following section.

The change in the color of the sample directly reflects the crystallization evolution of the samples derived from PMZrSZ2.5. Fig. 7 shows the XRD pattern evolution for ceramics derived from PMZrSZ2.5 (a) and PVMZrSZ2.5 (b) samples. Samples already crystallize after annealing at 1400 ˚C (PMZrSZ2.5_14 and PVMZrSZ2.5_14). Main sharp peaks corresponding to nanocrystalline phases appear at 33.8 ˚, 39.3 ˚, 56.75 ˚, 67.75 ˚, 71.15 ˚ and 84.5 ˚. The peaks matched with the rock salt ZrN phase (ICDD PDF number: 04-004-2860) in the cubic Fm-3 m space group. The crystallite sizes calculated at the dominant (111) peak were found to be 22.2 nm (PMZrSZ2.5_14) and 18.8 nm (PVMZrSZ2.5_14).

Annealing treatment also induces nucleation of α (ICDD PDF number: 04-005-5074) and β (ICDD PDF number: 04-033-1160) -Si_3N_4 in the PVMZrSZ2.5_14 sample, whereas there is only a very small contribution from crystalline silicon nitride in PMZrSZ2.5_14. Based on the Si-Ti-N systems that demonstrated a strong effect of the Ti content of the polymers on the crystallinity extent of the derived Si_3N_4 matrix [14], nucleation of Si_3N_4 already occurred at 1400 ˚C in the samples derived from PVMSZ, most probably because of the lowest Zr content in the material. After heat-treatment at 1500 ˚C, the XRD patterns show similar ZrN XRD peaks (in terms of FWHM and intensity) and the ZrN phase seems to be not affected by the increase of the annealing temperature. The ZrN crystallite calculated at the dominant (111) peak was found to be 22.2 nm (PMZrSZ2.5_15) and 20.8 nm (PVMZrSZ2.5_15); values close to those calculated for the samples prepared at 1400 ˚C. The continuous increase of the annealing temperature confirms the extended crystallization of the different constitutive phases as shown through the sharper and more intense ZrN peaks along with XRD peaks of α- and β-Si_3N_4 in the XRD patterns of samples annealed at 1600 ˚C (PMZrSZ2.5_16, ZrN crystallite size = 25.2 nm and PVMZrSZ2.5_16, ZrN crystallite size = 23.1 nm). It should be pointed out that the diffraction patterns in Fig. 7 do not indicate sample oxidation, which is generally evidenced by the broad shoulders of the ZrN (111) and (220) peaks [19]. For a better understanding of the structure and phase evolutions during annealing, the samples have been investigated by Raman spectroscopy (Fig. 9).

As illustrated in Fig. 9, the Raman spectra of the samples are characteristic of the face-centered cubic (*fcc*) ZrN phase through the presence of the low frequency (below 380 cm^{-1}; acoustic phonons) peaks - having the tendency to red-shift to higher frequency from 1400 to 1500 ˚C that could attest the improved crystallinity of the materials as well as the creation of N vacancies [49] in the nanocomposites - and high frequency (above 380 cm^{-1}; optical phonons) mode [50]. Interestingly,

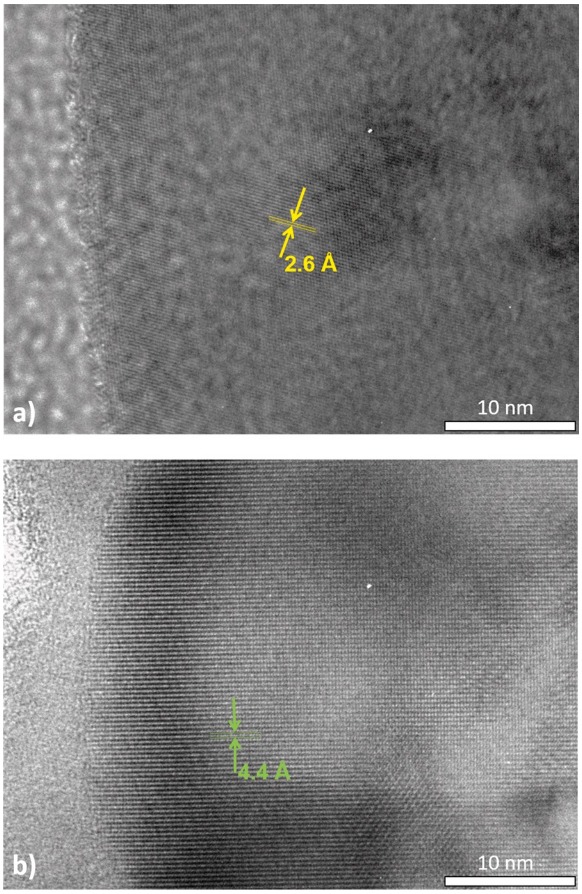

Fig. 11. HRTEM images of the PMZrSZ2.5_16 sample representing the fringe network of the ZrN (a) and α-Si$_3$N$_4$ (b) structures.

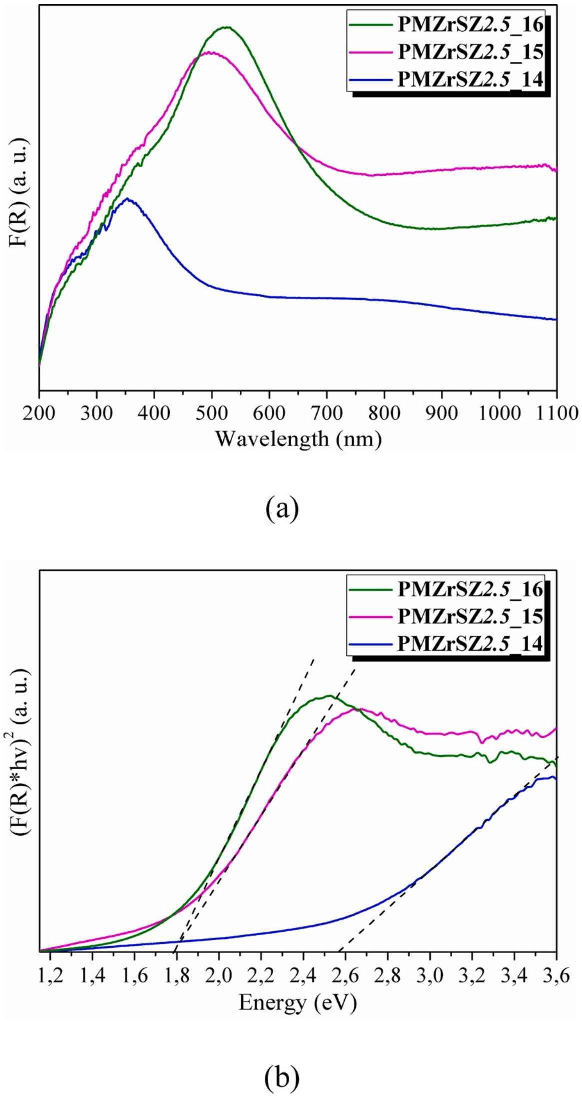

Fig. 12. (a) Plot of F(R) obtained from UV–vis diffused reflectance *versus* wavelength and (b) (F(R)-hν)^2 function *versus* photon energy (hν) for PMZrSZ2.5_14, PMZrSZ2.5_15 and PMZrSZ2.5_16.

there are one peak in the region 300–410 cm^{-1} between the acoustic and optic modes that tends to increase in intensity with the increase of the temperature of pyrolysis. It represents a low-frequency second-order acoustic mode (2A) and it is an indication of ZrN with less stoichiometric defects [51]. It should be mentioned that the Raman peak at 660 cm^{-1} - attributed to Si$_3$N$_4$ [52] and present in all spectra of the samples derived from PVMSZ, and in PMZrSZ2.5_15 and PMZrSZ2.5_16 samples - indicated that the Si$_3$N$_4$ crystallization occurred in such samples as observed in the XRD patterns.

The Raman spectrum of the PMZrSZ2.5_14 sample is quite different from other spectra. In particular, the bands in the high frequency mode above 380 cm^{-1} are shifted to higher frequencies most probably because of the poor crystallinity of the Si$_3$N$_4$ phase. The corresponding Raman peak is absent in the PMZrSZ2.5_14 sample, indicating that a crystallization of the Si$_3$N$_4$ matrix in all samples derived from PVMSZ, as well as in the PMZrSZ2.5_15 and PMZrSZ2.5_16 samples, most likely imposes a constraint state which affects the band positions of the ZrN phase in the Raman spectra. Therefore, based on the combination of XRD and Raman spectroscopy, we can conclude that the structure of ZrN/Si$_3$N$_4$ nanocomposites can be finely tailored through the chemistry of precursors from nanoscaled ZrN crystals distributed in an amorphous Si$_3$N$_4$ (PMZrSZ2.5_14 sample) to nanoscaled ZrN crystals distributed in a highly crystallized Si$_3$N$_4$ matrix (PMZrSZ2.5_16 and PVMZrSZ2.5_16 samples).

In order to assess the micro-/nanostructure of the latter, the PMZrSZ2.5_16 sample was further studied by means of HRTEM (Fig. 10a–d), in which the size population range of ZrN nanocrystals has been measured. The TEM micrographs (Fig. 10a and b) are consistent with the XRD data of the same sample: they indicate the formation of a highly crystallized material. The TEM micrograph, in Fig. 10c shows that the crystalline ZrN nanoparticles display a generally hexagonal shape which renders the generation of a particle size distribution highly complex from a series of low-magnification TEM images. The latter demonstrated that the particle size remains distributed over a relatively large range of diameter (See Fig. 4SI in ESI). The corresponding SAED pattern (Fig. 10d) and the EDS image (Fig. 10e) generated from the highlighted region align with standards for the lattice spacing of the ZrN (111), (200) and (220) planes, and confirm the presence of Zr and Si.

At higher magnification (Fig. 11), the HRTEM images show fringe spacing of 0.26 and 0.44 nm, corresponding to the d-spacing of the lattice plane of the ZrN and α-Si$_3$N$_4$ structures.

3.4. Optical properties of nanocomposites

The optical property is studied thoroughly due to the variable range of possible applications such as in LEDs, lasers, solar cells, photocatalysts, *etc* …. One of the most important parameters for determining the applicability of the title nanocomposites is their optical band gap (E_g), which means the minimum energy of light to be incident for the material to absorb the light and produce an electron - hole pair [53].

As a preliminary investigation, UV–vis spectroscopy was employed to examine the tuning of the ZrN/Si$_3$N$_4$ nanocomposite optical band gap.

Fig. 12 shows the optical properties of the samples derived from PMZrSZ*2.5*: PMZrSZ*2.5*_14, PMZrSZ*2.5*_15, and PMZrSZ*2.5*_16 over the UV–vis range (200–1100 nm).

Fig. 12a plots the Kubelka-Munk function *F(R)* [54] *versus* wavelength calculated from the recorded diffused reflectance spectra. The latter are characterized by a deep maximum of absorption in the UV (PMZrSZ*2.5*_14, 352 nm) and visible (PMZrSZ*2.5*_15 and PMZrSZ*2.5*_16, 498 and 524 nm, respectively) domains. Interestingly, Fig. 12a reveals the opportunities of tuning the optical properties as the annealing temperature increases, the position of the maximum of absorption increases and shifts towards higher wavelengths in line with the crystallization of the samples. The Kubelka-Munk method promotes the transformation of the measured diffuse reflectance and the extraction of the band gap (E_g) values with best accuracy [54,55]. After the Kubelka-Munk treatment shown in Fig. 12b, E_g value can be determined by extrapolating the linear least squares fit of $(F(R)h\nu)^2$ to zero, in a "$(F(R)h\nu)^2$ *versus* E" plot. Thus, by this method, the assignment of the optical band gap can be made (Fig. 12b) and we observed a decrease of the E_g values from 2.58 for PMZrSZ*2.5*_14 to 1.7 eV for PMZrSZ*2.5*_15 and PMZrSZ*2.5*_16. If we consider the PMZrSZ*2.5*_17 sample (samples annealed at 1700 °C), the band gap continues to decrease until reaches a value of 1.52 eV (See Fig. 5SI in ESI), unveiling the more conducting character of the latter. The calculated values are much lower than those found for bulk silicon nitride (5.0 eV) [56] and zirconium nitride (2.84–4.75 eV depending on the reactive gas) [57]. Thus, the crystallization of the different phases composing the nanocomposites, as well as their likelihood towards polymorphism (α- or β-Si_3N_4) and the increase in ZrN crystal size gives the annealing temperature a strong effect on the optical bandgap of the nanocomposites. This is especially compelling since it shows the possibility to tune the onset of the reflectance to the desired UV–vis wavelength. The reduced band gap of ZrN/Si_3N_4 nanocomposite prepared in the high temperature range (1600_1700 °C) is expected to improve their photocatalytic activities due the increase of their absorbance range from UV to visible in solar spectrum. Further works devoted to the photocatalytic activity of those materials are under investigation and will be published separately.

4. Conclusion

To summarize, we reported the synthesis of zirconium-modified polysilazanes by chemically modifying two polysilazanes, a polymethylsilazane (PMSZ) and a poly(vinylmethyl-*co*-methyl)silazane (PVMSZ), using tetrakis-(diethylamino)zirconium $Zr[N(CH_2CH_3)_2]_4$ with an atomic Si:Zr ratio of 2.5. The role of the chemistry behind the synthesis of these polymers was discussed based on complementary characterization tools, such as FTIR, solid-state NMR spectroscopy and elemental analyses. It corroborated our finding on Ti-modified polysilazanes: reactions mainly involved N–H and SiH– bonds in polysilazanes and $N(CH_2CH_3)$-based groups in $Zr[N(CH_2CH_3)_2]_4$ with a stronger contribution of Si–H bonds during the polymer synthesis and an important role of steric hindrance imposed by the vinyl groups in PVMSZ. Polymerization and/or hydrosilylation of vinyl groups present in PVMSZ could also occur during the synthesis of the polymers. Thus, the incorporation of Zr increased the crosslinking degree of the polysilazanes and introduced side groups that affected the weight change during the polymer-to-ceramic conversion under ammonia at 1000 °C, generating materials that were predominantly amorphous. Subsequent pyrolysis in the temperature range 1400_1600 °C under nitrogen allowed the precipitation of zirconium nitride nanocrystals embedded in a Si_3N_4 matrix. The crystallization (α- and β-Si_3N_4) of the latter closely depends on the Zr content of the considered polymers. HRTEM investigations highlighted the distribution of hexagonal faceted ZrN nanocrystals in the α- and β-Si_3N_4 matrix after heat-treatment at 1600 °C. The unique nano- and microstructural feature allowed tuning the ZrN/Si_3N_4 nanocomposite optical band gap as an interesting mean to explore the photocatalytic properties of these materials.

Data availability

Raw data and other supplementary material are available at the following repository: osf.io/7zpcj.

No data was used for the research described in the article.

Data will be made available on request.

No data was used for the research described in the article.

References

[1] D. Gielen, F. Boshell, D. Saygin, Climate and energy challenges for materials science, Nature Mater. 15 (2016) 117–120, https://doi.org/10.1038/nmat4545.

[2] O. Van der Biest, Nanoceramics: issues and opportunities, Inter. J. Appl. Ceram. Technol. 10 (2013) 565–576, https://doi.org/10.1111/ijac.12074.

[3] L. Dong, Y. Wang, X. Tong, T. Lei, Silicon carbide encapsulated graphite nanocomposites supported Pt nanoparticles as high-performance catalyst for methanol and ethanol oxidation reaction, Diamond Related Mater. 104 (2020) 107739–107744, https://doi.org/10.1016/j.diamond.2020.107739.

[4] Y. Feng, Y. Yang, Q. Wen, R. Riedel, Z. Yu, Dielectric properties and electromagnetic wave absorbing performance of single-source-precursor synthesized $Mo_{4.8}Si_3C_{0.6}$/SiC/C_{free} nanocomposites with an in situ formed nowotny phase, ACS. Appl. Mater. Int. 12 (2020) 16912–16921, https://doi.org/10.1021/acsami.0c01277.

[5] R. Kumar, M. Bahri, Y. Song, F. Gonell, C. Thomas, O. Ersen, C. Sanchez, C. Laberty-Robert, D. Portehault, Phase selective synthesis of nickel silicide nanocrystals in molten salts for electrocatalysis of the oxygen evolution reaction, Nanoscale 12 (2020) 15209–15213, https://doi.org/10.1039/D0NR04284F.

[6] E. Nyankson, J.K. Efavi, B. Agyei-Tuffour, G. Manu, Synthesis of TiO_2–Ag_3PO_4photocatalyst material with high adsorption capacity and photocatalytic activity: application in the removal of dyes and pesticides, RSC Adv. 11 (2021) 17032–17045, https://doi.org/10.1039/D1RA02128A.

[7] H. Wang, S. Zhu, J. Deng, W. Zhang, Y. Feng, J. Ma, Transition metal carbides in electrocatalytic oxygen evolution reaction, Chin. Chem. Lett. 32 (2021) 291–298, https://doi.org/10.1016/j.cclet.2020.02.018.

[8] X. Peng, C. Pi, X. Zhang, S. Li, K. Huo, P.K. Chu, Recent progress of transition metal nitrides for efficient electrocatalytic water splitting, Sustain. Energy Fuels 3 (2019) 366–381, https://doi.org/10.1039/C8SE00525G.

[9] M.I. Asghar, S. Jouttijärvi, P.D. Lund, High performance ceramic nanocomposite fuel cells utilizing LiNiCuZn-oxide anode based on slurry method, Int. J. Hydrogen Energy 43 (2018) 12797–12802, https://doi.org/10.1016/j.ijhydene.2018.03.232.

[10] A. Kovalčíková, J. Dusza, P. Šajgalík, Influence of the heat treatment on mechanical properties and oxidation resistance of SiC–Si_3N_4 composites, Ceram. Int. 39 (2013) 7951–7957, https://doi.org/10.1016/j.ceramint.2013.03.059.

[11] Y. Wang, W. Liu, J. Guo, M. Li, B. Fan, H. Wang, H. Xu, H. Lu, G. Shao, R. Zhang, L. An, In situ formation of Si_3N_4–SiC nanocomposites through polymer-derived SiAlCN ceramics and spark plasma sintering, Ceram. Int. 47 (2021) 22049–22054, https://doi.org/10.1016/j.ceramint.2021.04.225.

[12] A. Lale, M. Schmidt, M.D. Mallmann, A.V.A. Bezerra, E. Diz Acosta, R.A. F. Machado, U.B. Demirci, S. Bernard, Polymer-Derived Ceramics with engineered mesoporosity: from design to application in catalysis, Surf. Coat. Technol. 350 (2018) 569–586, https://doi.org/10.1016/j.surfcoat.2018.07.061.

[13] S. Tada, M.D. Mallmann, H. Takagi, J. Iihama, N. Asakuma, T. Asaka, Y. Daiko, S. Honda, R.K. Nishihora, R.A.F. Machado, S. Bernard, Y. Iwamoto, Low temperature in situ formation of cobalt in silicon nitride toward functional nitride nanocomposites, Chem. Commun. (2021) 2057–2060, https://doi.org/10.1039/d0cc07366k.

[14] M.C. Bechelany, V. Proust, A. Lale, P. Miele, S. Malo, C. Gervais, S. Bernard, Nanocomposites through chemistry of single-source precursors: understanding the role of chemistry behind the design of monolith-type nanostructured titanium nitride/silicon nitride, Chem. Eur. J. 23 (2017) 832–845, https://doi.org/10.1002/chem.201603661.

[15] A. Lale, M.D. Mallmann, S. Tada, A. Bruma, S. Özkar, R. Kumar, M. Haneda, R. A. Francisco Machado, Y. Iwamoto, U.B. Demirci, S. Bernard, Highly active, robust and reusable micro-/mesoporous TiN/Si_3N_4 nanocomposite-based catalysts: understanding the key role of TiN nanoclusters and amorphous Si_3N_4 matrix in the performance of the catalyst system, Appl. Catal. B Environ. 272 (2020) 118975–118984, https://doi.org/10.1016/j.apcatb.2020.118975.

[16] C. Zhou, A. Ott, R. Ishikawa, Y. Ikuhara, R. Riedel, E. Ionescu, Single-source-precursor synthesis and high-temperature evolution of novel mesoporous SiVN(O)-based ceramic nanocomposites, J. Eur. Ceram. Soc. 40 (2020) 6280–6287, https://doi.org/10.1016/j.jeurceramsoc.2019.11.021.

[17] Y. Yuan, J. Wang, S. Adimi, H. Shen, T. Thomas, R. Ma, J.P. Attfield, M. Yang, Zirconium nitride catalysts surpass platinum for oxygen reduction, Nat. Mater. 19 (2020) 282–286, https://doi.org/10.1038/s41563-019-0535-9.

[18] K. Chaudhuri, A. Shaltout, D. Shah, U. Guler, A. Dutta, V.M. Shalaev, A. Boltasseva, Photonic spin hall effect in robust phase gradient metasurfaces utilizing transition metal nitrides, ACS Photonics 6 (2019) 99–106, https://doi.org/10.1021/acsphotonics.8b00943.

[19] S. Exarhos, A. Alvarez-Barragan, E. Aytan, A.A. Balandin, L. Mangolini, Plasmonic core–shell zirconium nitride–silicon oxynitride nanoparticles, ACS Energy Lett. 3 (2018) 2349–2356, https://doi.org/10.1021/acsenergylett.8b01478.

[20] P. Patsalas, Zirconium nitride: a viable candidate for photonics and plasmonics? Thin Solid Films 688 (2019), 137438 https://doi.org/10.1016/j.tsf.2019.137438.

[21] M.C. Bechelany, V. Proust, C. Gervais, R. Ghisleni, S. Bernard, P. Miele, In-situ controlled growth of titanium nitride in amorphous silicon nitride: a general route toward bulk non-oxide nitride nanocomposites with very high hardness, Adv. Mater. 26 (2014) 6548–6553, https://doi.org/10.1002/adma.201402356.

[22] A. Lale, V. Proust, M.C. Bechelany, A. Viard, S. Malo, S. Bernard, A comprehensive study on the influence of the polyorganosilazane chemistry and material shape on the high temperature behavior of titanium nitride/silicon nitride nanocomposites, J. Eur. Ceram. Soc. 37 (2017) 5167–5175, https://doi.org/10.1016/j.jeurceramsoc.2017.04.001.

[23] M. Balestrat, A. Lale, A.V.A. Bezerra, V. Proust, E.W. Awin, R.A.F. Machado, P. Carles, R. Kumar, C. Gervais, S. Bernard, In-situ synthesis and characterization of nanocomposites in the Si-Ti-N and Si-Ti-C systems, Molecules 25 (2020) 5236–5258, https://doi.org/10.3390/molecules25225236.

[24] R.T. Paine, J.F. Janik, M. Fan, Some recent developments in precursor routes to ceramic nanocomposites, Polyhedron 13 (1994) 1225–1232, https://doi.org/10.1016/S0277-5387(00)80256-9.

[25] M. Weinmann, A. Zern, F. Aldinger, Stoichiometric silicon nitride/silicon carbide composites from polymeric precursors, Adv. Mater. 13 (2001) 1704–1708, https://doi.org/10.1002/1521-4095(200111)13:22%3C1704::AID-ADMA1704%3E3.0.CO;2-8.

[26] N. Hering, K. Schreiber, R. Riedel, O. Lichtenberger, J. Woltersdorf, Synthesis of polymeric precursors for the formation of nanocrystalline Ti-C-N/amorphous Si-C-N composites, Appl. Organomet. Chem. 15 (2001) 879–886, https://doi.org/10.1002/aoc.241.

[27] E. Ionescu, H.J. Kleebe, R. Riedel, Silicon-containing polymer-derived ceramic nanocomposites (PDC-NCs): preparative approaches and properties, Chem. Soc. Rev. 41 (2012) 5032–5052, https://doi.org/10.1039/C2CS15319J.

[28] G. Mera, M. Gallei, S. Bernard, E. Ionescu, Ceramic nanocomposites from tailor-made preceramic polymers, Nanomaterials 5 (2015) 468–540, https://doi.org/10.3390/nano5020468.

[29] E. Ionescu, B. Papendorf, H.J. Kleebe, F. Poli, K. Muller, R. Riedel, J. Am. Ceram. Soc. 93 (2010) 1774–1782, https://doi.org/10.1111/j.1551-2916.2010.03765.x.

[30] J. Yuan, S. Hapis, H. Breitzke, Y. Xu, C. Fasel, H.-J. Kleebe, G. Buntkowsky, R. Riedel, E. Ionescu, Single-source-precursor synthesis of hafnium-containing ultrahigh-temperature ceramic nanocomposites (UHTC-NCs), Inorg. Chem. 53 (2014) 10443–10455, https://doi.org/10.1021/ic501512p.

[31] Q.B. Wen, Y.P. Xu, B.B. Xu, C. Fasel, O. Guillon, G. Buntkowsky, Z.J. Yu, R. Riedel, E. Ionescu, Single-source-precursor synthesis of dense SiC/$HfC_xN_{1\_x}$-based ultrahigh-temperature ceramic nanocomposites, Nanoscale 6 (2014) 13678–13689, https://doi.org/10.1039/C4NR03376K.

[32] C. Zhou, X. Gao, Y. Xu, G. Buntkowsky, Y. Ikuhara, R. Riedel, E. Ionescu, Synthesis and high-temperature evolution of single-phase amorphous Si–Hf–N ceramics, J. Eur. Ceram. Soc. 35 (2015) 2007–2015, https://doi.org/10.1016/j.jeurceramsoc.2015.01.026.

[33] E.W. Awin, A. Lale, K.C.H. Kumar, U.B. Demirci, S. Bernard, R. Kumar, Plasmon enhanced visible light photocatalytic activity in polymer-derived TiN/Si-O-C-N nanocomposites, Mater. Des. 157 (2018) 87–96, https://doi.org/10.1016/j.matdes.2018.06.060.

[34] Q.B. Wen, Z.J. Yu, Y.P. Xu, Y. Lu, C. Fasel, K. Morita, O. Guillon, G. Buntkowsky, E. Ionescu, R. Riede, SiC/$Hf_yTa_{1-y}C_xN_{1-x}$/C ceramic nanocomposites with $Hf_yTa_{1-y}C_xN_{1-x}$-carbon core–shell nanostructure and the influence of the carbon-shell thickness on electrical properties, J. Mater. Chem. C 6 (2018) 855–864, https://doi.org/10.1039/C7TC05023B.

[35] S. Bhaskar, E.W. Awin, K.C. Hari Kumar, A. Lale, S. Bernard, R. Kumar, Design of nanoscaled heterojunctions in precursor-derived t-ZrO_2/SiOC(N) nanocomposites: transgressing the boundaries of catalytic activity from UV to visible light, Sci. Rep. 10 (2020) 430, https://doi.org/10.1038/s41598-019-57394-8.

[36] E.W. Awin, A. Lale, K.C.H. Kumar, S. Bernard, R. Kumar, Disordered mesoporous polymer derived N-doped TiO_2/Si-O-C-N nanocomposites with nanoscaled heterojunctions towards enhanced adsorption and harnessing of visible light, Appl. Surf. Sci. 508 (2020) 144953–144961, https://doi.org/10.1016/j.apsusc.2019.144953.

[37] E. Ionescu, S. Bernard, R. Lucas, P. Kroll, S. Ushakov, A. Navrotsky, R. Riedel, Ultrahigh temperature ceramics (UHTCs) and related materials – syntheses from polymeric precursors and energetics, Adv. Eng. Mater. 21 (2019) 1900269–1900292, https://doi.org/10.1002/adem.201900269.

[38] A. Viard, D. Fonblanc, M. Schmidt, A. Lale, C. Salameh, A. Soleilhavoup, M. Wynn, P. Champagne, S. Cerneaux, F. Babonneau, G. Chollon, F. Rossignol, C. Gervais, S. Bernard, Molecular chemistry and engineering of boron-modified polyorganosilazanes as new processable and functional SiBCN precursors, Chem. Eur. J. 23 (2017) 9076, https://doi.org/10.1002/chem.201700623.

[39] D. Fonblanc, D. Lopez-Ferber, M. Wynn, A. Lale, A. Soleilhavoup, A. Leriche, Y. Iwamoto, F. Rossignol, C. Gervais, S. Bernard, Crosslinking chemistry of poly(vinylmethyl-co-methyl)silazanes toward low-temperature formable preceramic polymers as precursors of functional aluminium-modified Si-C-N ceramics, Dalton Trans. 47 (2018) 14580–14593, https://doi.org/10.1039/C8DT03076F.

[40] D. Massiot, F. Fayon, M. Capron, I. King, S. Le Calvé, B. Alonso, J.-O. Durand, B. Bujoli, Z. Gan, G. Hoatson, Modelling one and two-dimensional solid-state NMR spectra, Magn. Reson. Chem. 40 (2002) 70–76, https://doi.org/10.1002/mrc.984.

[41] L. Gottardo, S. Bernard, C. Gervais, K. Inzenhofer, G. Motz, M. Weinmann, C. Balan, P. Miele, Chemistry, structure and processability of boron-modified polysilazanes as tailored precursors of ceramic fibers, J. Mater. Chem. 22 (2012) 7739–7750, https://doi.org/10.1039/C2JM15919H.

[42] A. Viard, L. Gottardo, D. Lopez-Ferber, A. Soleilhavoup, C. Salameh, S. Samal, Y. Gueguen, T. Rouxel, G. Motz, F. Babonneau, C. Gervais, S. Bernard, Molecular design of melt-spinnable co-polymers as Si–B–C–N fiber precursors, Dalton Trans. 46 (2017) 13510–13523, https://doi.org/10.1039/C7DT02559A.

[43] L. Gottardo, S. Bernard, C. Gervais, M. Weinmann, P. Miele, Study of the intermediate pyrolysis steps and mechanism identification of polymer-derived SiBCN ceramics, J. Mater. Chem. 22 (2012) 17923–17933, https://doi.org/10.1039/C2JM32737F.

[44] J. Seitz, J. Bill, N. Egger, F. Aldinger, Structural investigations of Si/C/N-ceramics from polysilazane precursors by nuclear magnetic resonance, J. Eur. Ceram. Soc. 16 (1996) 885–891, https://doi.org/10.1016/0955-2219(96)00007-6.

[45] O. Lichtenberger, E. Pippel, J. Woltersdorf, R. Riedel, Formation of nanocrystalline titanium carbonitride by pyrolysis of poly(titanylcarbodiimide), Mater. Chem. Phys. 81 (2003) 195–201, https://doi.org/10.1016/S0254-0584(03)00185-8.

[46] C. Gervais, F. Babonneau, L. Ruwisch, R. Hauser, R. Riedel, Solid-state NMR investigations of the polymer route to SiBCN ceramics, Can. J. Chem. 81 (2003) 1359–1369, https://doi.org/10.1139/v03-167. NRC Research Press.

[47] N.S. Choong Kwet Yive, R.J.P. Corriu, D. Leclercq, P.H. Mutin, A. Vioux, Silicon carbonitride from polymeric precursors: thermal cross-linking and pyrolysis of oligosilazane model compounds, Chem. Mater. 4 (1992) 141–146, https://doi.org/10.1021/cm00019a029.

[48] N.S. Choong Kwet Yive, R.J.P. Corriu, D. Leclercq, P.H. Mutin, A. Vioux, Thermogravimetric analysis/mass spectrometry investigation of the thermal conversion of organosilicon precursors into ceramics under argon and ammonia. 2. Poly(silazanes), Chem. Mater. 4 (1992) 1263–1271, https://doi.org/10.1021/cm00024a028.

[49] C.P. Constable, J. Yarwood, W.D. Mu¨nz, Raman microscopic studies of PVD hard coatings, Surf. Coat. Technol. 116 (1999) 155–159, https://doi.org/10.1016/ S0257-8972(99)00072-9.

[50] A.N. Christensen, O.W. Dietrich, W. Kress, W.D. Teuchert, Phonon anomalies in transition-metal nitrides: ZrN, Phys. Rev. B 19 (1979) 5699–5703, https://doi.org/10.1103/PhysRevB.19.5699.

[51] T.F. Mokgadi, M.J. Madito, M. Mlambo, V.A. Skuratov, S.V. Motloung, T. T. Hlatshwayo, Slow and swift heavy ions irradiation of zirconium nitride (ZrN) and the migration behaviour of implanted Eu, Nucl. Instrum. Methods Phys. Res. B 461 (2019) 63–69.

[52] W.Y. Ching, Y.N. Xu, J.D. Gale, M. Ru¨hle, Ab-Initio total energy calculation of α- and β-silicon nitride and the derivation of effective pair potentials with application to lattice dynamics, J. Am. Ceram. Soc. 81 (1998) 3189–3196, https://doi.org/10.1111/j.1151-2916.1998.tb02755.x.

[53] A. Luque, A. Mart, Increasing the efficiency of ideal solar cells by photon induced transitions at intermediate levels, Phys. Rev. Lett. 78 (1997) 5014–5017, https://doi.org/10.1103/PhysRevLett.78.5014.

[54] A.E. Morales, E.S. Mora, U. Pal, Use of diffuse reflectance spectroscopy for optical characterization of un-supported nanostructures, Revista Mexicana de Fisica Supplement 53 (2007) 18–22.

[55] S. Suwanboon, P. Amornpitoksuk, A. Haidoux, J.C. Tedenac, Structural and optical properties of undoped and aluminium doped zinc oxide nanoparticles via

precipitation method at low temperature, J. Alloys Compd. 462 (2008) 335–339, https://doi.org/10.1016/j.jallcom.2007.08.048.

[56] N. Manavizadeh, A. Khodayari, E. Asi-Soleimani, Investigation of the properties of silicon nitride (SiN_x) thin films prepared by RF sputtering for application in solar cell technology, in: Springer, Berlin, Heidelberg, in: D.Y. Goswami, Y. Zhao (Eds.), Proceedings of ISES World Congress 2007, 1–5, 2008, pp. 1120–1122, https://doi.org/10.1007/978-3-540-75997-3_220.

[57] M. Laurikaitis, S. Burinskas, J. Dudonis, D. Milcius, Physical properties of zirconium oxynitride films deposited by reactive magnetron sputtering, J. Phys. Conf. Ser. 100 (2008), 082051, https://doi.org/10.1088/1742-6596/100/8/082051.

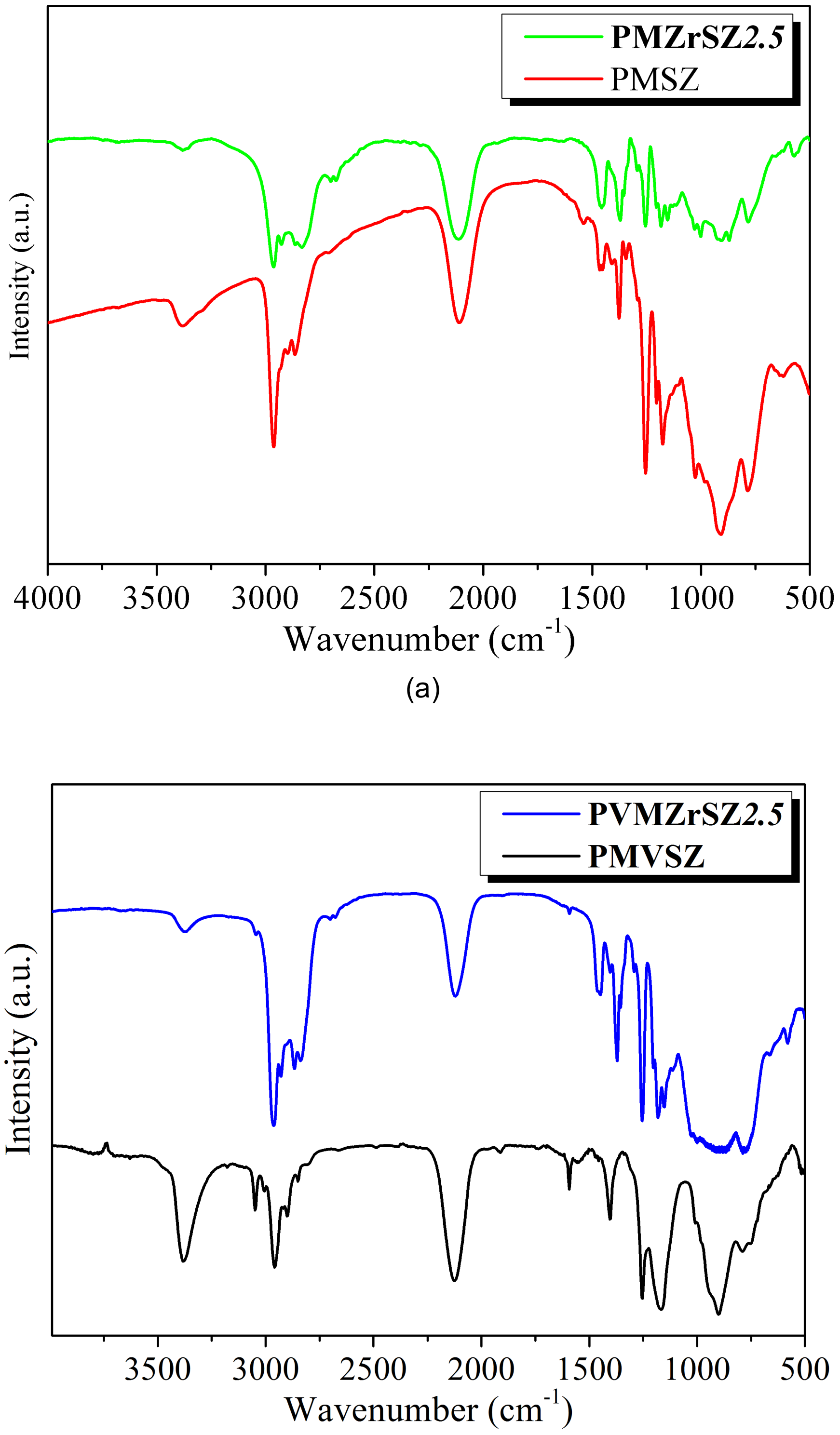

(a)

(b)

Fig. 1SI. FTIR spectra of (a) PMSZ and the derived **PMZrSZ*2.5*** and (b) PVMSZ and the derived **PVMZrSZ*2.5***.

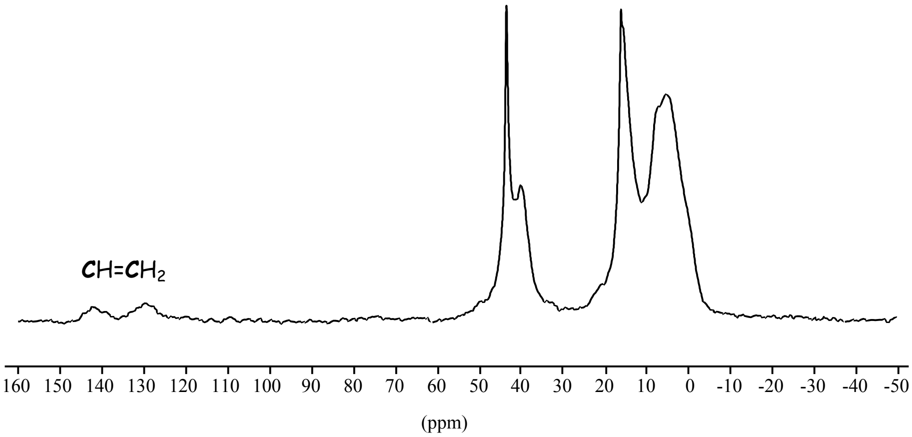

Fig. 2SI. Experimental ^{13}C CP MAS NMR recorded for the **PVMZrSZ*2.5*** sample from -50 to 160 ppm.

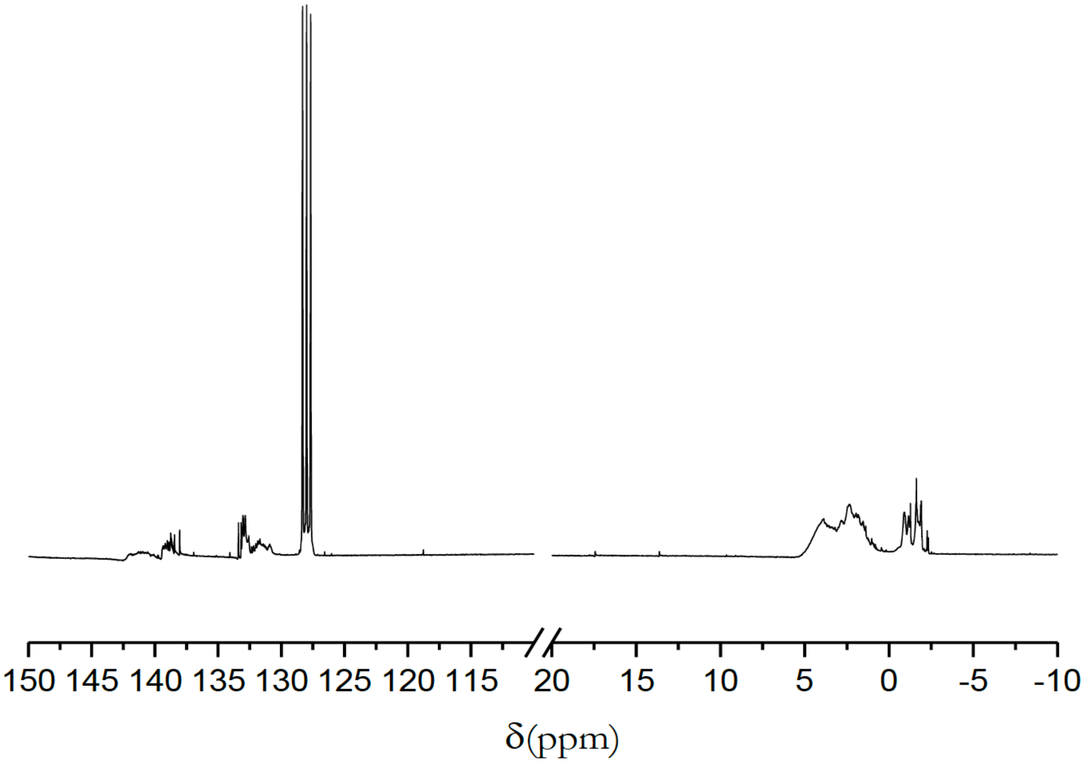

Fig. 3SI. Liquid-state ^{13}C NMR spectrum of PVMSZ.

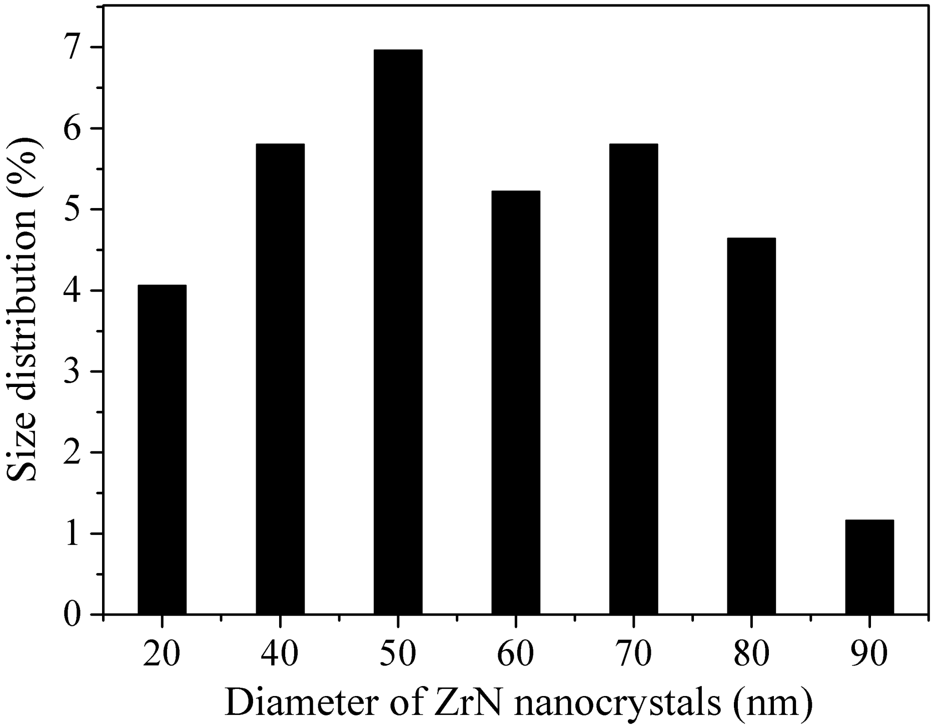

Fig. 4SI. Size distribution of ZrN nanocrystals calculated based on 62 measurements.

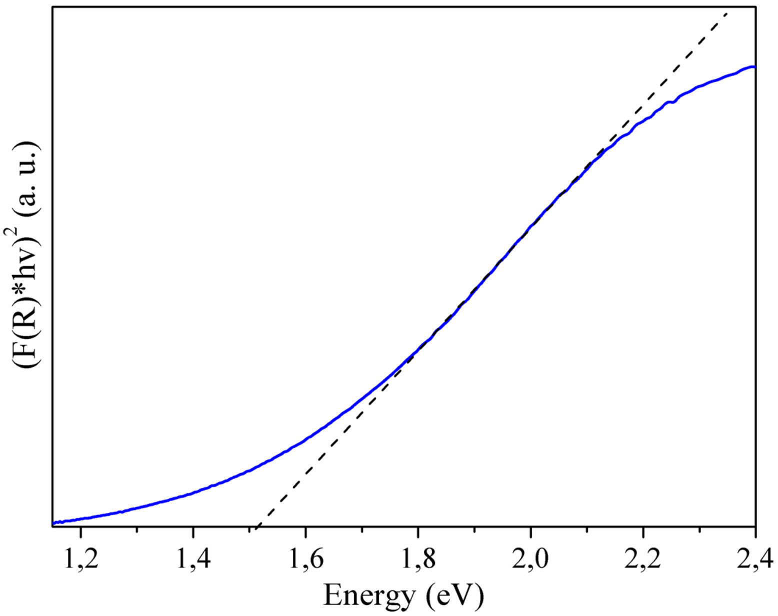

Fig. 5SI. $(F(R)*h\nu)^2$ function versus photon energy ($h\nu$) for **PMZrSZ*2.5*_17**.